A&A, 687, A70 (2024)
https://doi.org/10.1051/0004-6361/202449960

Astronomy & Astrophysics

Parsec-scale cosmic-ray ionisation rate in Orion

A. Socci[1], G. Sabatini[2], M. Padovani[2], S. Bovino[3,4,5], and A. Hacar[1]

[1] Institute for Astronomy (IfA), University of Vienna, Türkenschanzstrasse 17, 1180 Vienna, Austria
e-mail: andrea.socci@univie.ac.at
[2] INAF, Osservatorio Astrofisico di Arcetri, Largo E. Fermi 5, 50125 Firenze, Italy
[3] Chemistry Department, Sapienza University of Rome, P.le A. Moro, 00185 Rome, Italy
[4] INAF, Istituto di Radioastronomia, Via Gobetti 101, 40129 Bologna, Italy
[5] Departamento de Astronomía, Facultad Ciencias Físicas y Matemáticas, Universidad de Concepción Av. Esteban Iturra s/n Barrio Universitario, Casilla 160, Concepción, Chile

Received 13 March 2024 / Accepted 9 April 2024

ABSTRACT

Context. Cosmic rays are a key component of the interstellar medium because they regulate the dynamics and chemical processes in the densest and coldest regions of molecular clouds. Still, the cosmic-ray ionisation rate of H_2 ($\zeta_{H_2}^{ion}$) is one of the most debated parameters characterising molecular clouds because of the uncertainties in the adopted chemical networks and analysis techniques.

Aims. This work aims to homogeneously estimate the $\zeta_{H_2}^{ion}$ at parsec scales towards the Orion Molecular Clouds OMC-2 and OMC-3. We explore the change in $\zeta_{H_2}^{ion}$ across a whole star-forming region by probing a range of column densities that has never been explored before. The significant increase in statistics obtained by studying an entire region allows us to place stronger constraints on the range of $\zeta_{H_2}^{ion}$ values and exploit its connection with the physical properties of the interstellar medium.

Methods. The most recent $\zeta_{H_2}^{ion}$ estimates are based on o-H_2D^+, which is a direct product of the interaction between cosmic rays and H_2 in cold clouds. Since observations of o-H_2D^+ are challenging, we proxy its abundance through CO depletion by employing $C^{18}O$ (2–1) observations towards OMC-2 and OMC-3, taking advantage of the existing correlation between the two parameters. Using additional observations of HCO^+ (1–0) and DCO^+ (3–2), we determine the deuteration fraction, and we finally derive the map of $\zeta_{H_2}^{ion}$ in these two regions.

Results. The $C^{18}O$ depletion correlates with both the total column density of H_2 and the N_2H^+ emission across OMC-2 and OMC-3. The obtained depletion factors and deuteration fractions are consistent with previous values obtained in low- and high-mass star-forming regions. These two parameters additionally show a positive correlation in the coldest fields of our maps. We derive cosmic-ray ionisation rates of $\zeta_{H_2}^{ion} \sim 5 \times 10^{-18}$–$10^{-16}$ s^{-1}. These values agree well with previous estimates based on o-H_2D^+ observations. The $\zeta_{H_2}^{ion}$ also shows a functional dependence on the column density of H_2 across a full order of magnitude ($\sim 10^{22}$–10^{23} cm^{-2}). The estimated values of $\zeta_{H_2}^{ion}$ decrease overall for increasing $N(H_2)$, as predicted by theoretical models.

Conclusions. The results delivered by our approach are comparable with theoretical predictions and previous independent studies. This confirms the robustness of the analytical framework and promotes CO depletion as a viable proxy of o-H_2D^+. We also explore the main limitations of the method by varying the physical size of the gas crossed by the cosmic rays (i.e. the path length). By employing a path length obtained from low-resolution observations, we recover values of the $\zeta_{H_2}^{ion}$ that are well below any existing theoretical and observational prediction. This discrepancy highlights the need for interferometric observations in order to reliably constrain the $\zeta_{H_2}^{ion}$ at parsec scales as well.

Key words. astrochemistry – molecular data – cosmic rays – ISM: molecules

1. Introduction

Cosmic rays (CRs) are a fundamental component of the interstellar medium (ISM), but they may be the most puzzling component as well. Low-energy CRs ($E < 1$ TeV) can penetrate the cold ($T \lesssim 20$ K), dense gas ($n \gtrsim 10^4$ cm^{-3}) of molecular clouds and interact with H_2. The chain reactions following the H_2 ionisation produce H_3^+ (see Indriolo & McCall 2012, for a review), a key molecule for the production of most ionic species within molecular clouds (Herbst & Klemperer 1973). The number of ions over the number of neutral species, namely the ionisation fraction, is of paramount importance for star formation because it regulates the coupling between magnetic fields and the gas (Padovani et al. 2020), which may slow down or even halt the gravitational collapse of the cloud (Bergin & Tafalla 2007). In addition, the number of ions, H_3^+ in particular, drives the chemical evolution of the coldest regions within a cloud (e.g. Caselli & Ceccarelli 2012). However, while observed in infrared absorption in diffuse clouds (Indriolo & McCall 2012; Oka et al. 2019), H_3^+ cannot be detected in the millimeter regime, preventing a direct measure of the degree of ionisation in dense molecular clouds. The cosmic-ray ionisation rate (CRIR) is directly connected to H_3^+ and has been therefore determined over the years through several proxies, such as radicals (Black & Dalgarno 1977), ions (Caselli et al. 1998; Ceccarelli et al. 2014a; Redaelli et al. 2021b), neutrals (Fontani et al. 2017; Favre et al. 2018), and a combination of the latter (e.g. Luo et al. 2023). The values of CRIR determined in molecular clouds span three orders of magnitude ($\sim 10^{-17}$–10^{-14} s^{-1}) and show a dependence on the column density of H_2, $N(H_2)$, as expected from theoretical models (Padovani et al. 2009, 2022). The variety of techniques (most of them model dependent), tracers, and resolutions, however, makes for

an inhomogeneous sample of scattered estimates, especially in dense clouds ($N(H_2) \gtrsim 10^{22}$ cm^{-2}; e.g. Bovino & Grassi 2024).

Bovino et al. (2020) recently proposed o-H_2D^+ (hereafter o-H_2D^+) as a proxy for the CRIR relative to molecular hydrogen ($\zeta_{H_2}^{ion}$). H_2D^+ is the first product of the deuteration of H_3^+ and its ortho form was successfully detected in the millimeter regime at both low (Caselli et al. 2003, 2008; Giannetti et al. 2019; Sabatini et al. 2020; Miettinen 2020; Bovino et al. 2021) and high resolution (Redaelli et al. 2021a, 2022; Sabatini et al. 2023). Because the deuterium enrichment is favoured in cold dense gas (Millar et al. 1989; Walmsley et al. 2004), o-H_2D^+ is a reliable proxy of the $\zeta_{H_2}^{ion}$ in young pre-stellar environments ($t \lesssim 0.2$ Myr; Bovino et al. 2020). This analytic derivation was recently employed by Sabatini et al. (2020) and Sabatini et al. (2023), who determined $\zeta_{H_2}^{ion}$ from o-H_2D^+ in a sample of high-mass clumps and cores. The ionisation rates obtained by the authors are consistent with the theoretical predictions for a high-density regime (Padovani et al. 2024). Whilst the estimated $\zeta_{H_2}^{ion}$ reproduces the theoretical expectations, the detection of o-H_2D^+ has been a challenge for more than a decade (e.g. Caselli et al. 2008). As a consequence, the method proposed by Bovino et al. (2020) has only been applied to a limited range of column densities and scales, in particular, for $N(H_2) \gtrsim 10^{23}$ cm^{-2} and $R \lesssim 0.5$ pc (Sabatini et al. 2023).

We aim to derive the column density of o-H_2D^+ and then the $\zeta_{H_2}^{ion}$ for column densities within $N(H_2) \sim 10^{22}$–10^{23} cm^{-2} and for volume densities around $n \sim 10^5$ cm^{-3}. In the cold gas of molecular clouds where these volume densities are achieved, CO depletes onto dust grains, ions become abundant, and deuteration processes are boosted in general (Caselli & Ceccarelli 2012). In this context, the abundance of H_2D^+ is expected to grow for increasing depletion factors, as is also observed in different samples of both low- (Caselli et al. 2008) and high-mass (Sabatini et al. 2020) star-forming regions. Following previous studies, we determine N(o-H_2D^+) from the $C^{18}O$ depletion factor to provide an independent estimate of $\zeta_{H_2}^{ion}$ on parsec scales. Despite its limitations, which are discussed throughout the paper, our approach produces results that are consistent with previous works while at the same time, extending the dynamic range of column densities in the $\zeta_{H_2}^{ion}$ estimation.

The paper is then structured as follows: We introduce the method for the $\zeta_{H_2}^{ion}$ determination and its main assumptions (Sect. 2). We then present the observations, both novel (Sect. 3.1) and archival (Sect. 3.2), which are used throughout the paper, and we desscribe the related source selection. We next describe the analysis and results obtained for the degree of depletion (Sect. 4.1), the expected abundance of o-H_2D^+ (Sect. 4.2), the deuteration fraction (Sect. 4.3), and the ionisation rate (Sect. 4.6), along with their error budget (Sect. 4.5) and the limits of applicability (Sect. 4.4). Finally, we discuss the connection between $\zeta_{H_2}^{ion}$ and N(H_2) based on our analysis and in comparison with the theoretical predictions, together with the main limitations on the ionisation rate estimate (Sect. 5). Section 6 presents the main findings of our study.

2. Method

The method introduced by Bovino et al. (2020) provides a model-independent analytical expression for estimating $\zeta_{H_2}^{ion}$, which reads as follows (see also Sabatini et al. 2023):

$$\zeta_{H_2}^{ion} = k_{CO}^{o\text{-}H_3^+} \frac{N(\text{o-}H_2D^+) \times N(CO)}{3\, R_D \times N(H_2) \times l}. \quad (1)$$

In this equation: $k_{CO}^{o\text{-}H_3^+}$ is the destruction rate of o-H_3^+ by CO, considered here as main destruction path for o-H_3^+ (Redaelli et al. 2024); N(CO) is the total column density of CO; R_D (=$N(DCO^+)/N(HCO^+)$) is the deuteration fraction; l is the path length over which CO is depleted, and over which we estimate the column densities of our tracers; and N(o-H_2D^+) and $N(H_2)$ are the column densities of o-H_2D^+ and H_2, respectively.

The robustness and reliability of Eq. (1) have recently been confirmed by Redaelli et al. (2024) through synthetic observations of the molecular tracers simulated in a three-dimensional grid. The analysis provided $\zeta_{H_2}^{ion}$ estimates that are accurate within a factor of 2–3 compared to the input value of the simulation. These findings confirm the confidence level suggested by Bovino et al. (2020) for the method.

To apply Eq. (1), we relied on two main assumptions. First, we assumed o-H_2D^+ to be efficiently traced by the $C^{18}O$ depletion factor (f_D). This hypothesis is based on the correlation between the o-H_2D^+ abundance and the degree of CO depletion, a result that was consistently derived in earlier studies through observations (e.g. Crapsi et al. 2005; Caselli et al. 2008; Sabatini et al. 2020) and through theoretical predictions (e.g. Sipilä et al. 2015; Bovino et al. 2019). We therefore proxy the abundance of o-H_2D^+ via f_D using the correlation reported by Sabatini et al. (2020).

Second, we made an assumption on the path length l in Eq. (1). This path length is the physical extent of the o-H_2D^+ emission along the line of sight. Largely unknown, l is usually taken as the physical size of the o-H_2D^+ emission in the plane of the sky (e.g. Sabatini et al. 2023) or in the box where it is simulated (e.g. Redaelli et al. 2024), and it constitutes one of the main limitations of our method. We used $l = 0.050 \pm 0.015$ pc, the typical width of filamentary substructures seen in N_2H^+ in the Orion Molecular Clouds OMC-2 and OMC-3 (Socci et al. 2024). The molecular ion N_2H^+ becomes abundant when CO freezes-out on grains (Bergin & Tafalla 2007) and its emission has been proven to correlate with that of o-H_2D^+ (Redaelli et al. 2022). Thus, we take it as the representative scale for our study. Although unresolved in our observations (see Sect. 3.1), this scale is the most accurate estimate in the regions without relying on direct o-H_2D^+ observations. In Sect. 5, we discuss how different assumptions on l affect the determination of $\zeta_{H_2}^{ion}$.

3. Observations

3.1. IRAM-30m observations

Applying the method from Bovino et al. (2020) to estimate $\zeta_{H_2}^{ion}$ outside high-mass cores and clumps implies exploring column densities $N(H_2) \lesssim 10^{23}$ cm^{-2} at parsec scales. To fulfil this goal, the intregral shaped filament (ISF) in Orion (Bally et al. 1987) appeared as a natural choice. The ISF is a ~13 pc long filament in the Orion A molecular cloud. It is prominent in both dust continuum (e.g. Johnstone & Bally 1999) and molecular lines (e.g. Bally et al. 1987), and it is composed by several condensations, the OMCs (see Bally 2008, for a review). The ISF is also the closest site of high-mass star-formation in the Solar neighbourhood (414 pc; Menten et al. 2007) harbouring the Orion Nebula Cluster (ONC; Hillenbrand & Hartmann 1998) within OMC-1. The extended size, the wide dynamic range in H_2 column densities, and the connection to high-mass star formation make the ISF the best candidate for our study.

We surveyed OMC-1, OMC-2, OMC-3, and OMC-4 in $C^{18}O$ (2–1) (219.560 GHz), DCO^+ (3–2) (216.113 GHz), and HCO^+ (1–0) (89.189 GHz) using single-dish observations at 1mm and

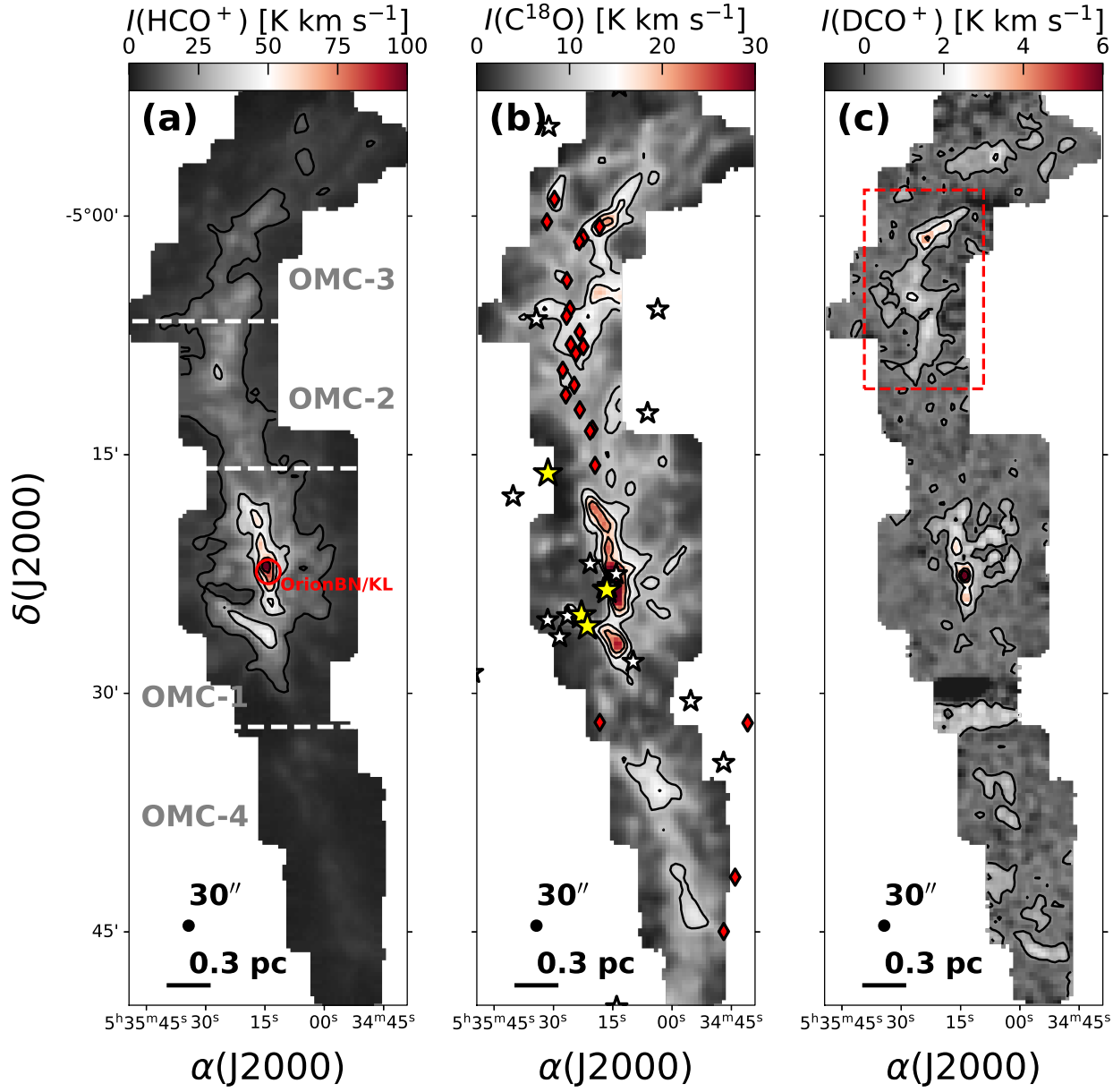

Fig. 1. Integral shaped filament as seen through our suite of tracers. *Panel a*: HCO^+ (1–0) integrated-intensity map of the four OMCs composing the ISF (separated by white lines; Bally 2008). The contours correspond to [10, 30, 50, 70, 90] K km s^{-1}. The red circle represents the position of the Orion BN/KL object. *Panel b*: $C^{18}O$ (2–1) integrated-intensity map of the OMCs composing the ISF. We include the O-type (yellow stars) and B-type (white stars) stars in the region, gathered from the SIMBAD Astronomical Database (Wenger et al. 2000), and the outflows detected by Tanabe et al. (2019) (red diamonds; see text for full discussion). The contours correspond to [10, 15, 20] K km s^{-1}. *Panel c*: DCO^+ (3–2) integrated-intensity map of the OMCs composing the ISF. The contours correspond to [0.5, 2, 4, 6] K km s^{-1}, where the lowest contour corresponds to a signal-to-noise ratio of 3. The red box is the region selected for the analysis, comprising part of OMC-2 and the whole OMC-3 (see text for a discussion).

3 mm. The observations were carried out at the 30-metre Institut de Radioastronomie Millimétrique telescope (IRAM-30 m) in Granada (Spain) during November 2013 (Project: 032-13, PI: A. Hacar). The large-scale IRAM-30 m mosaics centred on Orion BN/KL (Genzel & Stutzki 1989, α(J2000),δ(J2000) = 05h:35m:14s.20, −05°22′21″.5; see Fig. 1, panel a) were obtained with single 200″ × 200″ or 100″ × 100″ Nyquist-sampled on-the-fly (OTF) maps in position switching (PSw) mode (see Hacar et al. 2017, 2020, for additional information on the observations). Our suite of tracers have been observed with the same receiver, the Eight Mixer Receiver (EMIR; Carter et al. 2012), but with different backends: $C^{18}O$ (2–1) was observed with the VErsatile SPectrometer Array (VESPA) at a resolution of 20 kHz (∼0.027 km s^{-1} at 219.560 GHz), while DCO^+ (3–2) and HCO^+ (1–0) were observed with the Fast Fourier Transform Spectrometer (FTS; Klein et al. 2012) at a resolution of 200 kHz (∼0.27 km s^{-1} at 216.113 GHz and ∼0.66 km s^{-1} at 89.189 GHz, respectively). The spectra obtained in antenna temperature (T_a^*) were converted into main beam temperature (T_{mb}) with the relation $T_{mb} = T_a^* F_{ef}/B_{ef}$. Here, we used the standard forward (F_{ef}) and backward (B_{ef}) efficiencies for the IRAM-30m telescope[1] ($C^{18}O$ (2–1): B_{ef} = 0.61, F_{ef} = 0.93;

[1] https://publicwiki.iram.es/Iram30mEfficiencies

HCO^+ (1–0): B_{ef} = 0.81, F_{ef} = 0.95; DCO^+ (3–2): B_{ef} = 0.62, F_{ef} = 0.93). Finally, all the observations were convolved to a final resolution of 30″ (∼0.06 pc at the Orion distance). Figure 1 shows the integrated-intensity maps of the three molecules obtained by integrating the spectral cubes in the same velocity range ΔV_{lsr} = [6, 15] km s^{-1}, around the typical velocity expected for the ISF (V_{lsr} ∼ 10 km s^{-1}; Bally 2008). Similarly, the rms noise was estimated across the whole map, integrated in spectral windows with same velocity range but devoid of emission.

$C^{18}O$ and HCO^+ are readily detected and show widespread emission across the ISF. The high-sensitivity IRAM-30 m observations grant a peak-to-noise dynamic range of ≳100 for the intensities of both tracers. The more extended component of $C^{18}O$ and HCO^+ emission across the ISF shows values of ∼6–10 K km s^{-1} on average. These values increase along the ISF crest up to peaks of ∼35 K km s^{-1} for $C^{18}O$ and ∼100 K km s^{-1}, for HCO^+, seen towards OMC-1. DCO^+, on the other hand, shows a limited peak-to-noise dynamic range of ∼50, along with a patchy and uneven emission across the ISF. The few peaks with intensities of ≳4 K km s^{-1} are localised towards OMC-1 and OMC-2/OMC-3. All three tracers show their peak intensities towards OMC-1, where the radiation from the Trapezium stars (Hillenbrand 1997) and the ONC heats up the gas to temperatures above ∼40 K (Friesen et al. 2017). While all tracers share OMC-1 as the region of peak intensity, the $C^{18}O$ emission is often anti-correlated across the ISF compared to the emission of HCO^+. This change in morphology is prominent towards two regions: first, along OMC-2/OMC-3, where the $C^{18}O$ emission is scattered and fragmented, while HCO^+ shows a coherent filamentary shape (see Fig. 1, panels a, b); and second, in OMC-4, where the $C^{18}O$ emission is instead brighter than that of HCO^+. The behaviour in OMC-2/OMC-3 is of interest as it indicates extended $C^{18}O$ depletion in these two regions.

3.2. Archival observations and source selection

The ISF is a well-known region with a plethora of archival data. For our study, we took advantage of a few of these ancillary observations with a resolution comparable to that of our data. Among these, we are interested in a $N(H_2)$ map of the region to determine the candidate sites for depletion. Large-scale depletion is in fact expected for column densities $N(H_2) \gtrsim 10^{22}$ cm^{-2} (Bergin & Tafalla 2007; Tafalla et al. 2023). The column density map of H_2 was obtained from the 850 μm dust opacity, observed by the *Herschel* and *Planck* observatories, following the prescriptions of Lombardi et al. (2014) (see also Appendix A). Figure A.1, panel a, shows the ISF as seen in column density of H_2 (36.2″). The map shows material with column densities $N(H_2) \geq 10^{22}$ cm^{-2} extended across the whole filament with peaks of $N(H_2) \sim 10^{23}$ cm^{-2} along its crest, in correspondence to the OMCs. We focus on these regions, where the column density has a dynamic range of almost two orders of magnitude, and strong CO depletion is expected.

As mentioned in the previous section, N_2H^+ emission is strongly anti-correlated with CO emission because it is destroyed by the latter (e.g. Tobin et al. 2013). To further assess the presence of large-scale depletion in the ISF, we qualitatively compared the total column density of H_2 with the IRAM-30 m observations of N_2H^+ (1–0) from Hacar et al. (2017) (Fig. A.1, panel b). Although not as extended as the material with $N(H_2) \sim 10^{22}$ cm^{-2}, the N_2H^+ emission is widespread across the ISF and is closely correlated with $N(H_2)$ towards the OMCs (panel a). All four regions are thus candidates for efficient depletion, and as a consequence, they are good targets for estimating $\zeta_{H_2}^{ion}$.

Our focus instead shifted towards OMC-2 and OMC-3 alone, as suggested above. There are two main reasons for considering these two of the four OMCs. First, the OMC-1 region hosts several O-B stars (stars in Fig. 1, panel b; Wenger et al. 2000) and a plethora of highly embedded outflows (e.g. Rivilla et al. 2013). The radiation and heating from these objects can modify the $C^{18}O$ abundance by its selective photodissociation or its release in the gas phase from the ice coatings of dust grains (see Draine 2011, for a more thorough discussion). For a reliable estimate of the depletion, we excluded OMC-1, where the above processes are the most efficient in the ISF. Second, DCO^+ (3–2) emits weakly across the ISF (see Sect. 3.1), and in particular, there is no emission above a signal-to-noise ratio of 3 towards OMC-4. We are therefore limited in our analysis to OMC-2 and OMC-3 (see Peterson & Megeath 2008, for a review).

OMC-2 and OMC-3 themselves show variation of more than an order of magnitude in $N(H_2)$ and temperatures between T ∼ 10–40 K, according to different estimates (Friesen et al. 2017; Hacar et al. 2020). Because outflows are also detected in these two regions (diamonds in Fig. 1, panel b; Tanabe et al. 2019), we minimised their contamination to the $C^{18}O$ depletion estimate by imposing a temperature cut in the analysis of T_K = 10–25 K (using $T_K(NH_3)$ at 32″, Fig. A.1, panel c; Friesen et al. 2017). Given the close correlation between NH_3 and N_2H^+ (e.g. Tafalla et al. 2002), we expect $T_K(NH_3)$ to be the representative temperature for the gas in which CO freezes out onto the grains. The range T_K = 10–25 K is consistent with previously explored ranges in studies of f_D in high-mass regions (e.g. Sabatini et al. 2019). In addition, ∼20–25 K corresponds to the temperature limit at which CO evaporates from dust grains (Bergin & Tafalla 2007) for the volume density regime expected here (i.e. $n \gtrsim 10^5$ cm^{-3}).

OMC-2 and OMC-3 match all the previous characteristics with a clear detection of DCO^+, a low number of O-B stars nearby, a few scattered outflows, column densities up to $N(H_2) \sim 10^{23}$ cm^{-2}, and temperatures mostly below ≲25 K. Throughout these ∼1–2 pc north of the ISF, we expect $C^{18}O$ to be depleted and not photodissociated by stellar activity. Under these conditions, the depletion is expected to correlate to the o-H_2D^+ abundance (Caselli et al. 2008; Sabatini et al. 2020), and it may therefore be used to estimate the $\zeta_{H_2}^{ion}$.

4. Analysis and results

4.1. Depletion map of OMC-2 and OMC-3

As we wish to determine the onset of depletion, is mandatory to properly estimate the column density of $C^{18}O$ ($N(C^{18}O)$). First insights for this come from the inspection of $I(C^{18}O)$ and $I(N_2H^+)$ and their comparison with $N(H_2)$. We can qualitatively explore the $N(H_2)$ regime for which $C^{18}O$ depletes by computing the temperature-corrected line intensity (Tafalla et al. 2021),

$$I_T = \frac{I}{J_\nu(T_K) - J_\nu(T_{bg})}. \quad (2)$$

Through Eq. (2), the column density of H_2 alone now contributes to the line excitation, and therefore, to its intensity I_T. Figure 2 shows the comparison between I_T and $N(H_2)$ for our suite of tracers. We focus on $C^{18}O$ (panel a) and N_2H^+ (panel b). These two tracers show a continuous distribution with $N(H_2)$, but they behave differently for increasing column

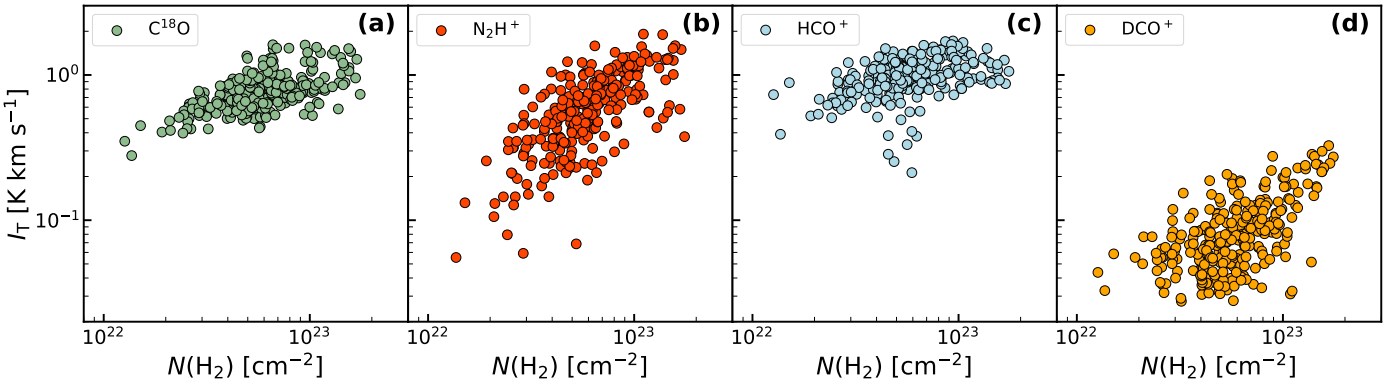

Fig. 2. Temperature-corrected integrated intensities (I_T) for our suite of tracers: $C^{18}O$ (*panel a*), N_2H^+ (*panel b*), HCO^+ (*panel c*), and DCO^+ (*panel d*). All the I_T values are computed following Tafalla et al. (2021) and are compared to $N(H_2)$ pixel by pixel (Lombardi et al. 2014).

densities. Across the dynamic range probed by our analysis ($N(H_2) \sim 10^{22}$–10^{23} cm^{-2}), the flattening of $I_T(C^{18}O)$, on one hand, and the linear increase in $I_T(N_2H^+)$, on the other hand, represent a clear chemical differentiation of the two tracers, in particular, of the effect of depletion on $C^{18}O$ (e.g. Tafalla et al. 2023).

To quantitatively describe the degree of $C^{18}O$ depletion in OMC-2 and OMC-3, we determined its column density ($N(C^{18}O)$). It can be computed as follows (Goldsmith & Langer 1999):

$$N_{\rm tot} = \frac{8\pi k\nu^2}{hc^3 A_{\rm ul}} \frac{Q(T_{\rm ex})\, e^{E_{\rm ul}/kT_{\rm ex}}}{g_{\rm u}} \frac{I\,\tau}{1-e^{-\tau}}, \quad (3)$$

with the corresponding parameters h, the Planck constant, k, the Boltzmann constant, c, the light speed, ν, the rest frequency of the line, $A_{\rm ul}$, the Einstein coefficient for spontaneous emission, Q, the partition function calculated at the excitation temperature of the line ($T_{\rm ex}$), $g_{\rm u}$, the degeneracy of the upper level, $E_{\rm u}$, the excitation energy of the upper level, and τ, the optical depth of the line. We can simplify the above equation for $N(C^{18}O)$ by introducing two approximations. First, we assume $C^{18}O$ (2–1) to be in local thermodynamic equilibrium (LTE) at the gas kinetic temperature T_K. Given the presence of N_2H^+ in the gas phase, the volume densities are expected to be $n \sim 10^5$ cm^{-3}, which is higher by at least an order of magnitude than the critical density of $C^{18}O$ (e.g. Tafalla et al. 2002). We therefore took $T_{\rm ex}(C^{18}O) = T_K(NH_3)$ for the rest of the analysis. Second, we work under the optically thin assumption (i.e. $\tau \ll 1$), adducing the flattening in $C^{18}O$ intensity only to its freeze-out onto the dust grains (see Tafalla et al. 2023, for a discussion). With these two approximations, Eq. (3) can be rewritten as

$$N_{\rm tot}(C^{18}O) \sim \frac{8\pi k\nu^2}{hc^3 A_{\rm ul}} \frac{Q(T_K)\, e^{E_{\rm ul}/kT_K}}{g_{\rm u}} I(C^{18}O). \quad (4)$$

The ratio of the expected abundance of $C^{18}O$ at the galactocentric distance of Orion (i.e. $X_0(C^{18}O) = 1.8 \times 10^{-7}$; Giannetti et al. 2017) and the abundance measured from the $C^{18}O$ column density ($X_{\rm obs} = N_{\rm tot}(C^{18}O)/N(H_2)$) gives the depletion factor

$$f_D = \frac{X_0}{X_{\rm obs}}. \quad (5)$$

Figure 3, panel a, shows this depletion factor, which, despite our source selection (see Sect. 3.2), is extended for ∼1 pc from OMC-2 to the tip of OMC-3. Depletion factors $f_D > 1$ correlate extremely well with N_2H^+ intensities above $I(N_2H^+) >$ 4 K km s^{-1} (signal-to-noise ratio of 10, black contours) and with the column densities $N(H_2) \gtrsim 10^{22}$ cm^{-2} in the two regions (see Fig. A.1). The depletion factors in our maps range from $f_D \sim$ 1–5, which is consistent with previous studies at comparable resolution (i.e. ∼30″) in infrared dark clouds (IRDCs; e.g. Hernandez et al. 2011; Sabatini et al. 2019), single low- (e.g. Crapsi et al. 2005) and high-mass (e.g. Fontani et al. 2006) star-forming regions. Similarly to these studies, we also determine fields in our map with f_D slightly below 1 (∼0.85 on average), which would imply an over-abundance of $C^{18}O$ compared to the expected X_0. Since these fields are restricted to the edges of the map, and given the small deviations from unity, these values $f_D < 1$ could result from uncertainties in their derivation rather than from a physical over-abundance of $C^{18}O$. We therefore masked these fields in Fig. 3, panel a, to consider only the regions in which depletion is effective ($f_D \geq 1$). This constrains our map to the filamentary structure that extends throughout OMC-2 and OMC-3.

4.2. Expected abundance of o-H_2D^+ on parsec scales

The challenging observations of o-H_2D^+ have limited its study to surveys of individual cores and clumps within low- (e.g. Caselli et al. 2008; Bovino et al. 2021) and high-mass (e.g. Sabatini et al. 2020; Redaelli et al. 2021a, 2022) star-forming regions. The opportunity to proxy its abundance with f_D, under proper conditions, opens up the path for parsec-scale studies of the ionisation processes. We thus applied the empirical correlation between f_D and X(o-H_2D^+) determined by Sabatini et al. (2020),

$$\log_{10}(X(\text{o-}H_2D^+)) = 0.05 \times f_D - 10.46. \quad (6)$$

Figure 3, panel b shows the X(o-H_2D^+) estimated with Eq. (6). The dynamic range of X(o-H_2D^+) is constrained within a factor of 3 (∼3–8 × 10^{-11}) and agrees excellently with the same abundances from Sabatini et al. (2020), as expected, because the depletion factors also agree well. These abundances of o-H_2D^+ are broadly consistent with independent estimates for low-mass cores (Caselli et al. 2008), but they are lower by an order of magnitude on average than the values determined for high-mass regions (Redaelli et al. 2021a; Sabatini et al. 2023). The difference between our estimates and those in high-mass regions can be explained by two main factors. First, the column densities probed in these regions ($N(H_2) \gtrsim 5 \times 10^{23}$ cm^{-2}) are higher compared to our work. The second factor is the beam dilution effect when comparing our low-resolution IRAM-30 m observations

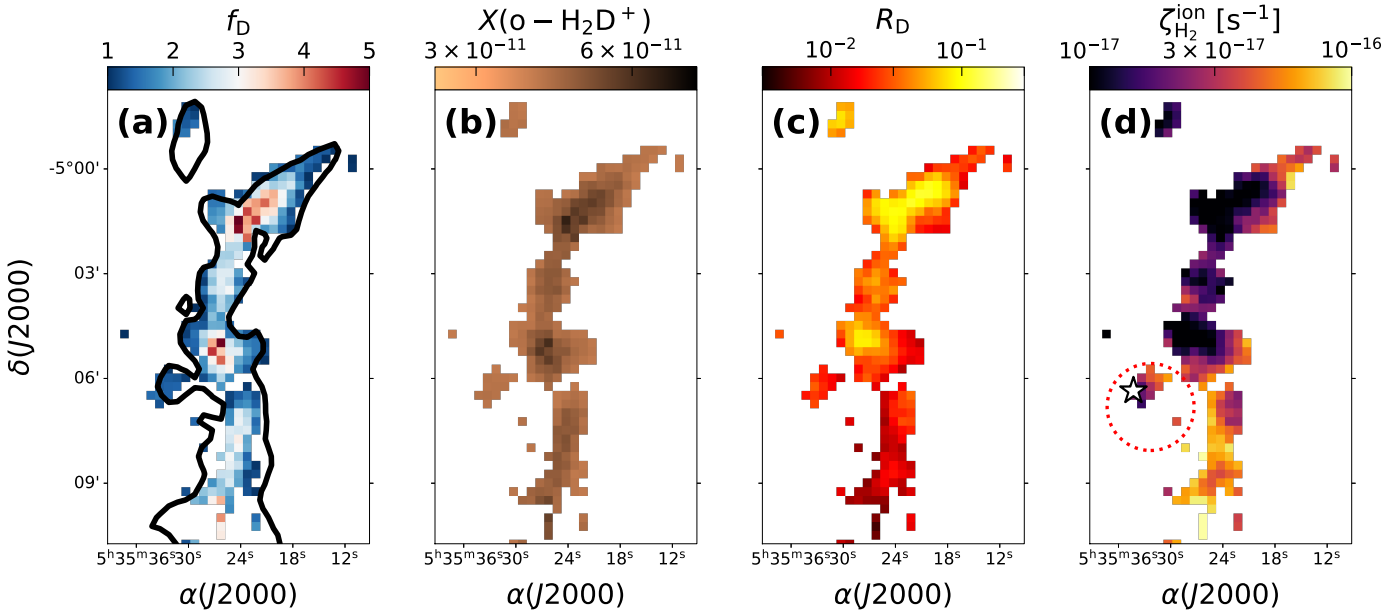

Fig. 3. Results for OMC-2 and OMC-3. *Panel a*: depletion map (f_D) obtained from the ratio of the expected abundance of $C^{18}O$ ($X_0(C^{18}O)$) in Orion and the measured abundance ($N_{tot}(C^{18}O)/N(H_2)$). The black contours represent $I(N_2H^+) > 4$ K km s^{-1} (signal-to-noise ratio of 10; see Fig. A.1, *panel b*). *Panel b*: abundance of o-H_2D^+ (X(o-H_2D^+)) inferred from the $C^{18}O$ depletion factor using the correlation from Sabatini et al. (2020). *Panel c*: deuteration fraction, determined as $R_D = N(DCO^+)/N(HCO^+)$, in OMC-2 and OMC-3 (see text for its determination). *Panel d*: $\zeta^{ion}_{H_2}$ determined with Eq. (1). The white star represents a B-type star within the selected region boundaries. The dotted red circle is a candidate expanding CO-shell (Feddersen et al. 2018) possibly connected to the star.

(30″) to their high-resolution ALMA observations (~2″). A comparison between observations and 3D modelling of the CO freeze-out suggests that depletion factors of $f_D \sim 3$–8 are typical at scales of ~0.1 pc (Bovino et al. 2019). These scales are close to the resolution of our maps (~0.06–0.07 pc), and therefore, X(o-H_2D^+) shows the same beam dilution effect as f_D, from which is inferred.

The o-H_2D^+ abundances we derived agree with those determined in previous studies for the most part. This highlights the CO depletion factor as a viable proxy for X(o-H_2D^+). However, independent measurements of these two parameters are needed to ultimately break the degeneracy and evaluate the empirical correlation found by Sabatini et al. (2020). The increasing sensitivity and spatial resolution of modern astronomical facilities, such as ALMA, will allow us to achieve this goal in the near future.

4.3. Deuteration fraction in OMC-2 and OMC-3

The deuteration fraction (R_D) is directly connected to all D-bearing isotopologues of H_3^+. These molecules are the main deuterium donors in the cold and dense gas of molecular clouds (e.g. Ceccarelli et al. 2014a). We estimated the deuteration fraction as $N(DCO^+)/N(HCO^+)$ through the DCO^+ (3–2) and HCO^+ (1–0) lines. Our first approach could again be to estimate the column densities of both tracers using Eq. (3) in the optically thin limit ($\tau \ll 1$) and to assume LTE at the kinetic temperature T_K. While reasonable for $C^{18}O$, the LTE assumption is not ideal for DCO^+ and HCO^+ because of the higher critical densities of these two molecules (e.g. Sanhueza et al. 2012; Keown et al. 2016). In addition, the HCO^+ (1–0) can easily become optically thick (e.g. Vasyunina et al. 2012), and therefore, a correction for τ is expected.

Similarly to $C^{18}O$, we inspected the temperature-corrected intensities of HCO^+ and DCO^+ and compared them to $N(H_2)$ (see Fig. 2). $I_T(HCO^+)$ (panel c) shows a clear dependence on $N(H_2)$ with a compact distribution. Only a handful of fields show significant scatter, which implies the almost complete absence of self-absorbed profiles in our sample (see Tafalla et al. 2023). However, while not self-absorbed, the HCO^+ intensities likely become opaque as the distribution flattens towards $N(H_2) \sim 10^{23}$ cm^{-2}. $I_T(DCO^+)$ (panel d) also clearly depends on $N(H_2)$. Compared to those of HCO^+, the intensities of DCO^+ increase almost linearly with $N(H_2)$ for a distribution resembling that of N_2H^+. However, $I_T(DCO^+)$ shows a higher degree of scatter compared to $I_T(N_2H^+)$, suggesting deviations from the LTE assumption used to apply Eq. (2).

To estimate the excitation effects on DCO^+ and HCO^+, we ran a grid of radiative transfer models for each pixel using RADEX (van der Tak et al. 2007) in two different steps[2]. In the first step, we input $N_{tot}(DCO^+)$ and $N_{tot}(HCO^+)$ calculated in the LTE optically thin limit and varied n, the volume density, in logarithmic intervals between 10^4 and 10^6 cm^{-3}. In the second step, we fixed these same volume densities and let the two column densities vary by an order of magnitude around the LTE optically thin values. We then took from the output of RADEX the two N_{tot} that minimised the observed intensities. In both steps, we input T_K as the kinetic temperature and fixed the line widths of DCO^+ and HCO^+ to $\Delta v = 0.75 \pm 0.10$ km s^{-1} and $\Delta v = 2.5 \pm 0.4$ km s^{-1}, respectively. These line widths are the mean values obtained by fitting a few representative spectra in our fields, and their error was taken as the standard deviation seen in these fits.

The deuteration fraction (Fig. 3, panel c) shows variation by more than an order of magnitude (~0.005–0.1) in OMC-2

[2] The radiative transfer calculations were not applied to $C^{18}O$ because without proper modelling of the cloud, which includes a freeze-out threshold, depletion may be mistaken for opacity (e.g. see Tafalla et al. 2021).

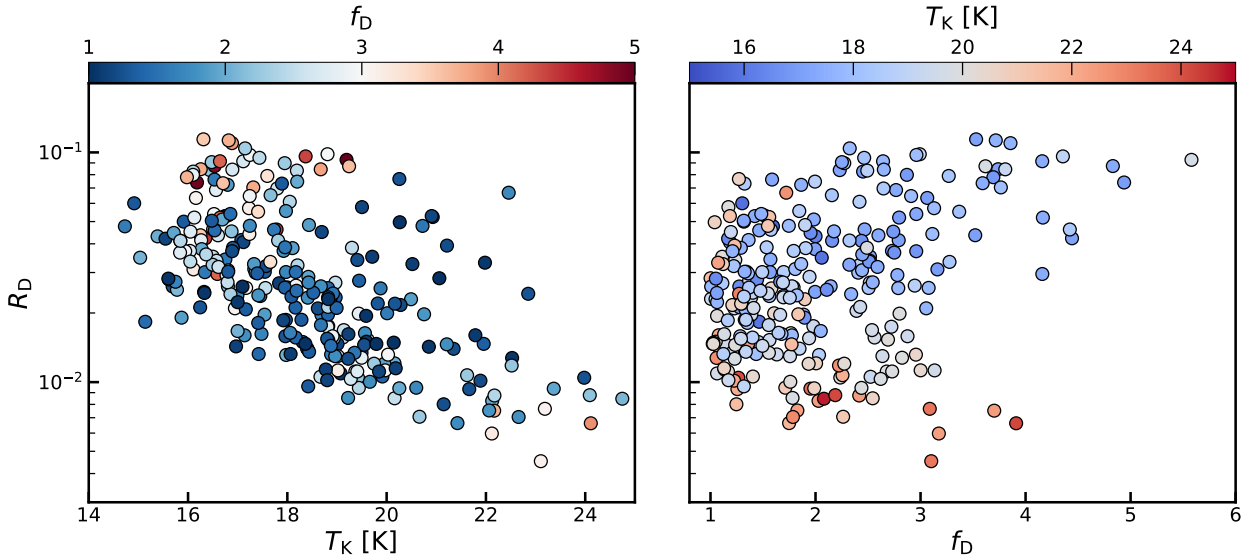

Fig. 4. Comparison between R_D, f_D and T_K in our targets. *Left panel*: deuteration fraction (R_D) compared to the kinetic temperature (T_K). Each point is colour-coded with the corresponding depletion factor (f_D). *Right panel*: deuteration fraction (R_D) now compared to the depletion factor (f_D) and colour-coded with the corresponding kinetic temperature (T_K).

and OMC-3. These values are consistent with previous studies in high-mass star-forming regions (Sabatini et al. 2020, 2023; Pazukhin et al. 2023), that used the same molecular species, and with theoretical predictions from chemical models (Albertsson et al. 2013). The connection found between f_D and R_D in these and other studies (e.g. in low-mass regions; Crapsi et al. 2005) demonstrates the enhancement of the deuteration process in the cold and dense gas where CO is depleted (e.g. Caselli & Ceccarelli 2012, for a review). Simulations of turbulent and magnetised parsec-scale filaments, such as the ISF (e.g. Pattle et al. 2017; Hacar et al. 2018; Zielinski & Wolf 2022), show increasing levels of deuteration as the column density increases (Körtgen et al. 2018). The simulations from Körtgen et al. determined deuteration fractions within ~0.01–0.1 on timescales $t \lesssim$ 0.4 Myr, which is consistent with the expected survival time of the dense gas in Orion (~0.5 Myr; Hacar et al. 2024). Since o-H_2D^+ is the driver of deuteration in the early phases of the cloud evolution (Bovino et al. 2020), and given the dependence between f_D and R_D, a correlation between X(o-H_2D^+) and f_D would be readily explained.

The variation in R_D in our maps shows a progressive increase from OMC-2 in the south to OMC-3 towards the north. This gradient reflects the morphology of the HCO^+ and DCO^+ integrated intensities shown in Figs. 1a, c. The variation could be linked to a change in volume density which would cause the higher-J levels of the two molecules to be more populated. The non-LTE analysis returns a limited range in volume densities, however, which varies within ~0.3–2 × 10^5 cm^{-3} (with mean value and standard deviation of $n = 1.0 \pm 0.2 \times 10^5$ cm^{-3}). Therefore, the significant variation in R_D is likely the result of a more efficient deuteration process towards OMC-3.

It is well known (since Watson 1974) that deuteration is affected by temperature variations, which cause a change in the reaction rates. The deuteration of HCO^+ into DCO^+ is particularly sensitive to this temperature effect (see Pazukhin et al. 2023, for a recent example). Thus, the gradient we observe in R_D is possibly linked to the slight change in T_K from OMC-3 to OMC-2 (see Fig. A.1, panel c). We explore this hypothesis in Fig. 4, where we display the comparison of R_D with T_K (left panel) and f_D (right panel). The left panel shows an anti-correlation between the deuteration fraction and the kinetic temperature that was also reported in previous studies (e.g. Pazukhin et al. 2023). This anti-correlation becomes most prominent for fields with low depletion factors ($f_D \lesssim 2$). When the temperatures increase towards and above $T_K \gtrsim 20$ K, the deuteration fraction drops to values of $\lesssim$0.01. For temperatures ~16–19 K, however, there is a significant scatter, for which the fields with higher depletion ($f_D \gtrsim$ 2–3) also show a higher degree of deuteration ($R_D \gtrsim 0.03$). These same points may be identified in the right panel and they show a positive correlation between R_D and f_D. This dependence between the two parameters was previously reported by Crapsi et al. (2005) for a similar range of values and volume density regime ($n \sim 10^5$ cm^{-3}). We therefore expect the correlation between R_D and f_D to be robust below $\lesssim$20 K and to become weaker for higher temperatures with the corresponding $\zeta_{H_2}^{ion}$ estimates possibly uncertain.

As a final test, we determined a scaling relation between R_D and T_K in Fig. B.1. First, we sampled the median value and interquartile range (IQR) of R_D and T_K in bins of 1 K (red circles and error bars, respectively). Then, we fitted a power-law dependence to these estimates, for which the best fit (black line) reads as $R_D \sim T_K^{-4}$ (see Eq. (B.1)). This sharp decrease in $R_D(HCO^+)$ with T_K was previously observed in different clouds (e.g. Pazukhin et al. 2023), but it was never before condensed in a scaling relation. The direct comparison of this scaling relation with estimates of $R_D(HCO^+)$ and T_K in massive clumps (Miettinen et al. 2011) and high-mass regions (Gerner et al. 2015) confirms the goodness of our fit (see the full discussion in Appendix B). The systematic nature of the effect, which appears to be independent from the star-formation regime of the region, suggests the use of temperature-corrected deuteration fractions for future estimates of $\zeta_{H_2}^{ion}$ using the method described in Sect. 2.

4.4. Destruction rate $k_{CO}^{o\text{-}H_3^+}$

Equation (1) assumes that o-H_3^+ is primarily destroyed by CO (Bovino et al. 2020; Redaelli et al. 2024). While this is one of

the main processes in dense cores, other destruction pathways can occur when the ionisation rate is studied at parsec scales. In particular, electrons can reduce the H_3^+ abundance through dissociative recombination. This process becomes important at extreme densities, when the CO is almost entirely depleted (e.g. Redaelli et al. 2024), and at lower densities, especially in the regions that are externally illuminated by stellar radiation, such as the ISF (e.g. Pabst et al. 2019).

We therefore considered estimates of the ionisation fraction, $x(e^-)$, in these two density regimes and compared them with the analytical limit $f_D < 9 \times 10^{-7}/x(e^-)$ proposed by Redaelli et al. (2024) for Eq. (1). First, we considered the estimates in massive dense cores, including some in Orion (Bergin et al. 1999). Bergin et al. estimated ionisation fractions $x(e^-) \lesssim 10^{-7}$ at $N(H_2) \gtrsim 10^{22}$ cm^{-2} for these sources, leading to a depletion limit for the method of $f_D \gtrsim 9$. Second, we considered the estimates in OMC-2 and OMC-3 using the C_2H and HCN lines (Salas et al. 2021). Salas et al. instead determined ionisation fractions $x(e^-) \leq 3 \times 10^{-6}$ at $n \sim 5 \times 10^3$ cm^{-3}, leading to an unphysical $f_D > 0.3$. Given our range in both column and volume density ($N(H_2) \sim 10^{22}$–10^{23} cm^{-2} and $n(H_2) \sim 0.3$–2×10^5 cm^{-3}, respectively), we can safely assume that the destruction through CO is the main process affecting the H_3^+ abundance for our degree of depletion.

We finally determined the destruction rate $k_{CO}^{o\text{-}H_3^+}$ in our regions. We computed the latter pixel by pixel using T_K and the coefficients found in the KInetic Database for Astrochemistry (KIDA[3]; Wakelam et al. 2012) for the ion-polar reaction $H_3^+ + CO \rightarrow HCO^+ + H_2$. The adopted $k_{CO}^{o\text{-}H_3^+}$ rates in the temperature range of 10–25 K are relatively constant and lie within ~ 2.15–2.35×10^{-9} cm^{-3} s^{-1}.

4.5. Error budget in the determination of $\zeta_{H_2}^{ion}$

Our indirect determination of $\zeta_{H_2}^{ion}$ presents a number of error sources that are discussed in the following. Excluding $X(o\text{-}H_2D^+)$, for which the CO depletion is assumed as an efficient proxy (see Sect. 2), all the other parameters in Eq. (1) bear a corresponding uncertainty, as we list below.

- $k_{CO}^{o\text{-}H_3^+}$, $N(C^{18}O)$ both only depend on the temperature (see Eq. (4) and Sect. 4.4). We therefore propagated their error accordingly using the uncertainty on T_K (Friesen et al. 2017).
- $[^{16}O]/[^{18}O]$ was used to convert $N(C^{18}O)$ into $N(CO)$ in Eq. (1). This parameter is equal to 560 ± 26 for the local ISM (see Table 4 in Wilson & Rood 1994).
- R_D has, given its definition and its derivation with RADEX, the combined uncertainties on the DCO^+ and HCO^+ line widths as the total uncertainty (see Sect. 4.3);
- l has the typical size of N_2H^+ structures in OMC-2 and OMC-3 (see Sect. 2), along with their corresponding error (see also Socci et al. 2024).

The error per field in our analysis reaches up to ∼50% of the corresponding $\zeta_{H_2}^{ion}$ in OMC-2 and OMC-3. However, this error contains a strong flat contribution from the conservative choices we made to estimate the uncertainty on some parameters (e.g. line widths of DCO^+ and HCO^+). A more thorough analysis would therefore significantly reduce the uncertainty in several of our fields. Since the determination of $\zeta_{H_2}^{ion}$ remains indirect and this error budget does not hinder our further discussion and conclusions, we continued with these choices for our analysis.

[3] https://kida.astrochem-tools.org

4.6. Cosmic-ray ionisation rate map of Orion

The map of $\zeta_{H_2}^{ion}$ (Fig. 3, panel d) shows a dynamic range of more than one order of magnitude in the OMC-2/OMC-3 region. The global south-north decrease in $\zeta_{H_2}^{ion}$ is likely connected to the gradient seen in the deuteration fraction, which is further connected to the effect of temperature (see Fig. 4, left panel). However, the local variations in $\zeta_{H_2}^{ion}$ are likely induced by the change in f_D throughout the filament (see Fig. 4, right panel). As a result of these two effects, $\zeta_{H_2}^{ion}$ varies within $\sim 5 \times 10^{-18}$–2×10^{-16} s^{-1} within the two regions.

The median value we derive of $\zeta_{H_2}^{ion} \sim 2.4 \times 10^{-17}$ s^{-1} agrees well with the estimates in high-mass star-forming regions using the same method (Sabatini et al. 2020, 2023). The slight differences reflect the variation in $X(o\text{-}H_2D^+)$ (see Sect. 4.2), which may be ascribed to a resolution effect. The highest values of $\zeta_{H_2}^{ion}$ we determine (i.e. $\gtrsim 2 \times 10^{-16}$ s^{-1}) are seen south of the map, and in particular, in the region close to the OMC-2 FIR4 protocluster (e.g. Johnstone et al. 2003) and the B-type star HD 37060 (see Fig. 3, panel d). These two heating sources can indirectly affect our estimate through an increase in T_K, with a corresponding decrease in R_D. In addition, the outflows from the protocluster (e.g. López-Sepulcre et al. 2013; Chahine et al. 2022) and the UV-irradiation from the star could promote the photodissociation of $C^{18}O$, inducing an increase in f_D (see Fig. 4, right panel). However, higher values of $\zeta_{H_2}^{ion}$ could also result from a local enhancement in the CR flux (see Padovani et al. 2015, 2016, 2019) caused by these objects, as suggested by previous findings: CRs ionisation rates as high as $\zeta_{H_2}^{ion} \sim 10^{-14}$ s^{-1} were previously reported in OMC-2 FIR4 (Ceccarelli et al. 2014b; Fontani et al. 2017). A candidate expanding CO-shell was detected in close correspondence to the B-type star (Feddersen et al. 2018), for which CRs could travel beyond its edge and promote the ionisation in the southern part of our filament.

Despite all the influences on the ionisation rate, $\zeta_{H_2}^{ion} \approx 10^{-17}$ s^{-1}, originally found by Spitzer & Tomasko (1968), was instead considered for several decades as the reference value for the ISM. While this value is reproduced by our results, our parsec-scale map shows variation of at least an order of magnitude for $\zeta_{H_2}^{ion}$ in OMC-2 and OMC-3. No constant value for the ionisation rate is therefore expected, but instead, local changes in the physical properties of the gas play a crucial role in its variation. Of the possible physical influences on the CR ionisation rate, we consider the effect of increasing $N(H_2)$ as the prime driver of its variation.

5. Discussion

The different models for the energy loss of CR particles (protons, electrons and heavy nuclei) with increasing $N(H_2)$ were originally studied by Padovani et al. (2009). These models account for the ionisation by primary CR protons and electrons, plus secondary electrons from primary CRs. For the column density regime we probed, the models of CR propagation (see Fig. 5, coloured lines) are largely dominated by CR protons and their secondaries. As a general trend, all models predict a decrease in $\zeta_{H_2}^{ion}$ with increasing $N(H_2)$. Different slopes come from the comparison between the CR propagation models and observational results: model $\mathscr{L}$, from the CR spectrum observed by the Voyager missions (Cummings et al. 2016; Stone et al. 2019); model $\mathscr{H}$, from the average ionisation rate estimated in diffuse clouds (Indriolo & McCall 2012; Neufeld & Wolfire 2017); and model

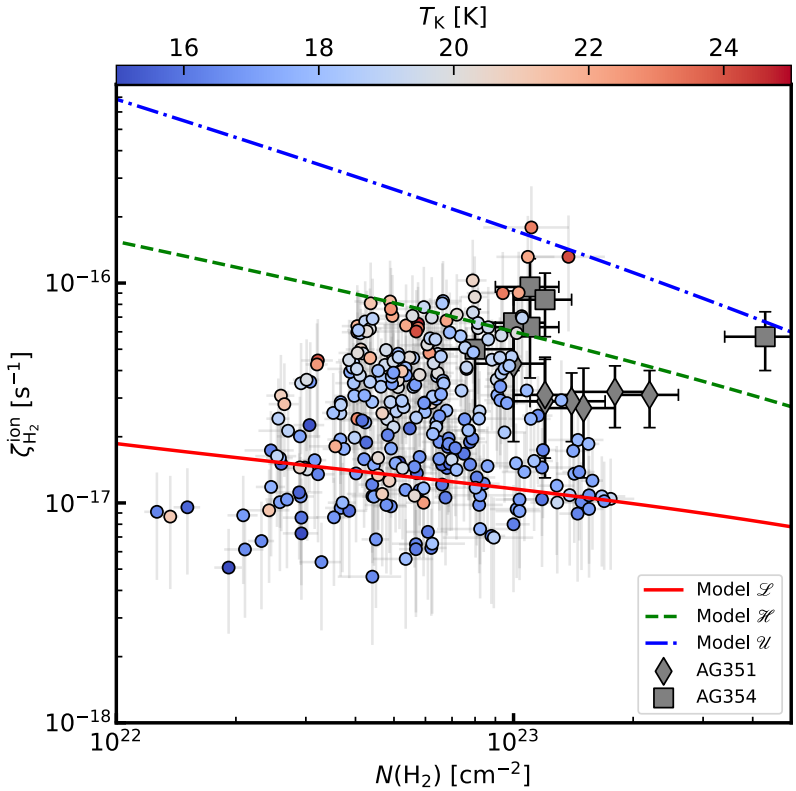

Fig. 5. Comparison between $\zeta_{H_2}^{ion}$ and the column density $N(H_2)$. The theoretical predictions for the CR propagation in molecular clouds are displayed as colour-coded lines (blue, green, and red lines; Padovani et al. 2022), while the $\zeta_{H_2}^{ion}$ estimates in high-mass regions are displayed in grey (squares and diamonds; Sabatini et al. 2023). The estimates of $\zeta_{H_2}^{ion}$ from our study are displayed as circles, colour-coded by T_K.

$\mathscr{U}$, from the upper limit of the ionisation rate in diffuse clouds. Observational results show a decreasing trend as well, but the large number of methods and tracers used to infer $\zeta_{H_2}^{ion}$ produces a significant scatter in the data, especially for dense clouds (see Fig. B.1 in Padovani et al. 2024).

Our new results considerably increase the statistics for the available $\zeta_{H_2}^{ion}$ estimates compared to previous studies (e.g. Caselli et al. 1998; van der Tak & van Dishoeck 2000). In particular, we probed the CR ionisation rate within a poorly explored column density regime. Figure 5 shows the comparison between $\zeta_{H_2}^{ion}$ and $N(H_2)$, colour-coded by T_K, with their corresponding errors (see Lombardi et al. 2014, and Sect. 4.5, respectively). In addition, we plot the models from Padovani et al. (2022) for different slopes of the CR proton energy spectrum (coloured lines). Almost the entire sample of $\zeta_{H_2}^{ion}$ determined in our study is enclosed within models $\mathscr{L}$ and $\mathscr{H}$, with only a fraction of fields outside of this range. Despite their departure from the bulk of our points, these ionisation rates above model $\mathscr{H}$ and below model $\mathscr{L}$ are still consistent with the theoretical predictions within the errors. None of the predicted propagation models clearly reproduces our results. Our estimates show the functional dependence between $\zeta_{H_2}^{ion}$ and $N(H_2)$ expected from these models, however. While the temperature dependence of R_D (see Sect. 4.3) contributes to the scatter, the fields with $T_K \lesssim 20$ K show decreasing ionisation rates for increasing $N(H_2)$.

As we included the $\zeta_{H_2}^{ion}$ determined in two high-mass star-forming regions using the same method (diamonds and squares; Sabatini et al. 2023), the ionisation rates in the two studies agree well. Our estimates show values closer to those in AG531 overall, while only the highest ionisation rates we determined are comparable to those in AG354. The combined distribution of ionisation rates from the two studies is continuous with $N(H_2)$ and mildly depends on it within $\sim 10^{22}$–5×10^{23} cm^{-2}. The method proposed by Bovino et al. (2020) therefore allows homogeneous estimates of $\zeta_{H_2}^{ion}$ in a wide range of scales and column density regimes, when o-H_2D^+ is either successfully detected or reasonably inferred.

The two estimates from our paper and Sabatini et al. (2023) agree well, but spurious effects have to be considered in their determination. While resolution affects the degree of depletion on the one hand (see Sect. 4.2), it also influences the minimum physical size we can probe with our observations on the other hand. This physical size is condensed in the path length l from Eq. (1). As mentioned in Sect. 2, it is complex to measure either the line-of-sight length or the volume density of the tracers, and therefore, l is usually taken as the radial size of the structures identified in o-H_2D^+ (Sabatini et al. 2020, 2023). We explored the influence of l on the $\zeta_{H_2}^{ion}$ by measuring the typical radial size of the DCO^+ emission, our least extended tracer. To do this, we performed a radial sampling on the DCO^+ integrated-intensity map following the peaks of its emission and fit the average profile with a Gaussian function (see Appendix A for a full discussion). The FWHM of the profile (0.18 ± 0.15 pc) was taken as representative l to compute the estimate of $\zeta_{H_2}^{ion}$. Since this FWHM is three to four times the l adopted in our analysis (0.05 pc; see Sect. 2), the corresponding $\zeta_{H_2}^{ion}$ values are lower by the same factor on average (see Eq. (1), $\zeta_{H_2}^{ion} \propto 1/l$). The median ionisation rate with $l \sim 0.18$ pc is $\zeta_{H_2}^{ion} \sim 7 \times 10^{-18}$ s^{-1}, and the majority of the fields is below model $\mathscr{L}$. Ionisation rates as low as $\sim 10^{-18}$ s^{-1}, produced by correspondingly low-energy CRs, are unrealistic when considering the degree of feedback present in the ISF (Pabst et al. 2019), and they strongly disagree with

independent estimates, which indeed suggest higher values (e.g. Fontani et al. 2017; Salas et al. 2021). As f_D and R_D are positively correlated, their ratio is only mildly affected by resolution effects. The path length, l, on the other hand, is directly affected by a poor resolution, and thus represents the main limitation in the determination of ionisation rates with Eq. (1) (see also Bovino et al. 2020; Redaelli et al. 2024, for different ways to estimate l and a detailed analysis on its effect to the $\zeta_{H_2}^{ion}$).

Our results highlight the CO depletion as available proxy for the o-H_2D^+ abundance at parsec scales. However, caution should be taken when interpreting these results: First, the determination of f_D can be hard and the use of multiple CO lines is usually advised (e.g. Sabatini et al. 2022). Second, the connection between f_D and the o-H_2D^+ abundance was derived at sub-parsec scales (Sabatini et al. 2020) and works within a constrained range of T_K, outside which multiple processes may become temperature dependent (e.g. the degree of deuteration). In turn, estimates based on o-H_2D^+ are confirmed as an effective method for the homogeneous sampling of $\zeta_{H_2}^{ion}$ over more than an order of magnitude in column density. Ultimately, in the absence of local sources of CRs, $N(H_2)$ alone appears to drive the ionisation degree in molecular clouds (Padovani et al. 2022). Finally, our results also highlight the importance of high-resolution observations to estimate the degree of depletion and to estimate l reliably. Both parameters can in fact significantly affect the determination of $\zeta_{H_2}^{ion}$. Independent interferometric observations of both CO isotopologues and o-H_2D^+ are needed to validate the previous correlation by Sabatini et al. (2020) and to provide a more robust estimate of the cosmic-ray ionisation rate.

6. Conclusions

We presented the first parsec-scale estimate of the cosmic-ray ionisation rate determined by employing the most recent analytical framework proposed by Bovino et al. (2020). To this end, we presented novel IRAM-30 m observations of the ISF in Orion using the following suite of tracers: $C^{18}O$ (2–1), DCO^+ (3–2) and HCO^+ (1–0). We first determined the $C^{18}O$ depletion factor under density and temperature regimes for which we expect significant freeze-out and no photodissociation effects. The $C^{18}O$ depletion factor was then used as a proxy of the o-H_2D^+ abundance, following the correlation determined by Sabatini et al. (2020) and to ultimately determine the ionisation rate $\zeta_{H_2}^{ion}$. The main results of the study are listed below:

- The depletion factor map is extended from north of OMC-2 to the tip of OMC-3 with values ranging within $f_D \sim 1$–5. This dynamic range is consistent with previous estimates for whole clouds (Hernandez et al. 2011; Sabatini et al. 2019; Feng et al. 2020) and within single star-forming regions (Crapsi et al. 2005; Fontani et al. 2006; Sabatini et al. 2022, 2023).
- The o-H_2D^+ abundance inferred from f_D has a constrained dynamic range between ~ 3–8×10^{-11}, in agreement with previous independent observations (Caselli et al. 2008; Giannetti et al. 2019; Miettinen 2020; Redaelli et al. 2021a; Sabatini et al. 2023). Although estimated indirectly, the good agreement of our X(o-H_2D^+) compared to those measured in these studies suggests that f_D is a reliable proxy, at least at the spatial scales we studied.
- The deuteration fraction (R_D) we determined shows values within ~0.005–0.1. These values are consistent with previous estimates using the same molecular species (Sabatini et al. 2023) and show a positive correlation with f_D for the volume density regime we explored ($n \sim 10^5$ cm^{-3}). A positive correlation between f_D and R_D was previously reported for similar volume densities (Crapsi et al. 2005). The deuteration fraction decreases with temperature, in particular for $T_K \gtrsim 20$ K. Below this value, its positive correlation with f_D is more robust.
- The map of $\zeta_{H_2}^{ion}$ shows a south-north gradient with values that vary within $\sim 5 \times 10^{-18}$–2×10^{-16} s^{-1}. This gradient is likely connected to the temperature dependence of R_D, but local variations, especially for $T_K \sim 16$–19 K are driven by the degree of depletion. The wide dynamic range in $\zeta_{H_2}^{ion}$ overall is ascribed to the variation of local physical properties (e.g. $N(H_2)$), as expected from theoretical models (Padovani et al. 2009).
- The ionisation rates we determined for the column density regime we probed ($\sim 10^{22}$–2×10^{23} cm^{-2}) are comparable to the theoretical predictions for the same column densities (Padovani et al. 2022). They are mildly anti-correlated with the column density, as expected from the models of CR propagation within clouds, extended to values of $N(H_2) \gtrsim 10^{23}$ cm^{-2} when complemented by the estimates of Sabatini et al. (2023).
- Finally, we tested the influence of the estimated path length l on $\zeta_{H_2}^{ion}$. When the path length is directly determined from our low-resolution DCO^+ observations, its value is ~0.18 pc. This l produces results no longer consistent with those in high-mass regions (Sabatini et al. 2023) and with independent studies in the ISF (e.g. Fontani et al. 2017) when applied to our analysis. In addition, these lower ionisation rates are only marginally reproduced by the theoretical predictions (Padovani et al. 2022). All these discrepancies suggest that high-resolution data are needed to provide reliable estimates of l. This path length becomes otherwise the main limiting factor in the determination of the CR ionisation rates.

Acknowledgements. The authors thank the anonymous referee for their suggestions to improve the manuscript. This project has received funding from the European Research Council (ERC) under the European Union's Horizon 2020 research and innovation programme (Grant agreement No. 851435). GS acknowledges the projects PRIN-MUR 2020 MUR BEYOND-2p ("Astrochemistry beyond the second period elements", Prot. 2020AFB3FX) and INAF-Minigrant 2023 TRIESTE ("TRacing the chemIcal hEritage of our originS: from proTo-stars to planEts"; PI: G. Sabatini). SB acknowledges the ANID BASAL project FB210003. This work is based on IRAM-30 m telescope observations carried out under project numbers 032-13. IRAM is supported by INSU/CNRS (France), MPG (Germany), and IGN (Spain). This research has made use of the SIMBAD database, operated at CDS, Strasbourg, France. This research has made use of NASA's Astrophysics Data System.

References

Albertsson, T., Semenov, D. A., Vasyunin, A. I., Henning, T., & Herbst, E. 2013, ApJS, 207, 27
Bally, J. 2008, in Handbook of Star Forming Regions, Volume I, 4, ed. B. Reipurth, 459
Bally, J., Langer, W. D., Stark, A. A., & Wilson, R. W. 1987, ApJ, 312, L45
Bergin, E. A., & Tafalla, M. 2007, ARA&A, 45, 339
Bergin, E. A., Plume, R., Williams, J. P., & Myers, P. C. 1999, ApJ, 512, 724
Black, J. H., & Dalgarno, A. 1977, ApJS, 34, 405
Bohlin, R. C., Savage, B. D., & Drake, J. F. 1978, ApJ, 224, 132
Bovino, S., & Grassi, T. 2024, Astrochemical Modeling: Practical Aspects of Microphysics in Numerical Simulations (Elsevier)
Bovino, S., Ferrada-Chamorro, S., Lupi, A., et al. 2019, ApJ, 887, 224
Bovino, S., Ferrada-Chamorro, S., Lupi, A., Schleicher, D. R. G., & Caselli, P. 2020, MNRAS, 495, L7
Bovino, S., Lupi, A., Giannetti, A., et al. 2021, A&A, 654, A34
Carter, M., Lazareff, B., Maier, D., et al. 2012, A&A, 538, A89
Caselli, P., & Ceccarelli, C. 2012, A&A Rev., 20, 56

Caselli, P., Myers, P. C., & Thaddeus, P. 1995, ApJ, 455, L77
Caselli, P., Walmsley, C. M., Terzieva, R., & Herbst, E. 1998, ApJ, 499, 234
Caselli, P., van der Tak, F. F. S., Ceccarelli, C., & Bacmann, A. 2003, A&A, 403, L37
Caselli, P., Vastel, C., Ceccarelli, C., et al. 2008, A&A, 492, 703
Ceccarelli, C., Caselli, P., Bockelée-Morvan, D., et al. 2014a, in Protostars and Planets VI, eds. H. Beuther, R. S. Klessen, C. P. Dullemond, & T. Henning, 859
Ceccarelli, C., Dominik, C., López-Sepulcre, A., et al. 2014b, ApJ, 790, L1
Chahine, L., López-Sepulcre, A., Podio, L., et al. 2022, A&A, 667, A6
Crapsi, A., Caselli, P., Walmsley, C. M., et al. 2005, ApJ, 619, 379
Cummings, A. C., Stone, E. C., Heikkila, B. C., et al. 2016, ApJ, 831, 18
Draine, B. T. 2011, Physics of the Interstellar and Intergalactic Medium
Favre, C., Ceccarelli, C., López-Sepulcre, A., et al. 2018, ApJ, 859, 136
Feddersen, J. R., Arce, H. G., Kong, S., et al. 2018, ApJ, 862, 121
Feng, S., Li, D., Caselli, P., et al. 2020, ApJ, 901, 145
Fontani, F., Caselli, P., Crapsi, A., et al. 2006, A&A, 460, 709
Fontani, F., Ceccarelli, C., Favre, C., et al. 2017, A&A, 605, A57
Friesen, R. K., Pineda, J. E., co-PIs, et al. 2017, ApJ, 843, 63
Genzel, R., & Stutzki, J. 1989, ARA&A, 27, 41
Gerner, T., Beuther, H., Semenov, D., et al. 2014, A&A, 563, A97
Gerner, T., Shirley, Y. L., Beuther, H., et al. 2015, A&A, 579, A80
Giannetti, A., Leurini, S., König, C., et al. 2017, A&A, 606, L12
Giannetti, A., Bovino, S., Caselli, P., et al. 2019, A&A, 621, L7
Goldsmith, P. F., & Langer, W. D. 1999, ApJ, 517, 209
Hacar, A., Alves, J., Tafalla, M., & Goicoechea, J. R. 2017, A&A, 602, L2
Hacar, A., Tafalla, M., Forbrich, J., et al. 2018, A&A, 610, A77
Hacar, A., Bosman, A. D., & van Dishoeck, E. F. 2020, A&A, 635, A4
Hacar, A., Socci, A., Bonanomi, F., et al. 2024, A&A, in press https://doi.org/10.1051/0004-6361/202348565
Herbst, E., & Klemperer, W. 1973, ApJ, 185, 505
Hernandez, A. K., Tan, J. C., Caselli, P., et al. 2011, ApJ, 738, 11
Hillenbrand, L. A. 1997, AJ, 113, 1733
Hillenbrand, L. A., & Hartmann, L. W. 1998, ApJ, 492, 540
Indriolo, N., & McCall, B. J. 2012, ApJ, 745, 91
Johnstone, D., & Bally, J. 1999, ApJ, 510, L49
Johnstone, D., Boonman, A. M. S., & van Dishoeck, E. F. 2003, A&A, 412, 157
Keown, J., Schnee, S., Bourke, T. L., et al. 2016, ApJ, 833, 97
Klein, B., Hochgürtel, S., Krämer, I., et al. 2012, A&A, 542, L3
Körtgen, B., Bovino, S., Schleicher, D. R. G., et al. 2018, MNRAS, 478, 95
Lombardi, M., Bouy, H., Alves, J., & Lada, C. J. 2014, A&A, 566, A45
López-Sepulcre, A., Taquet, V., Sánchez-Monge, Á., et al. 2013, A&A, 556, A62
Luo, G., Zhang, Z.-Y., Bisbas, T. G., et al. 2023, ApJ, 946, 91
Menten, K. M., Reid, M. J., Forbrich, J., & Brunthaler, A. 2007, A&A, 474, 515
Miettinen, O. 2020, A&A, 634, A115
Miettinen, O., Hennemann, M., & Linz, H. 2011, A&A, 534, A134
Millar, T. J., Bennett, A., & Herbst, E. 1989, ApJ, 340, 906
Neufeld, D. A., & Wolfire, M. G. 2017, ApJ, 845, 163
Oka, T., Geballe, T. R., Goto, M., et al. 2019, ApJ, 883, 54
Pabst, C., Higgins, R., Goicoechea, J. R., et al. 2019, Nature, 565, 618
Padovani, M., Galli, D., & Glassgold, A. E. 2009, A&A, 501, 619
Padovani, M., Hennebelle, P., Marcowith, A., & Ferrière, K. 2015, A&A, 582, L13
Padovani, M., Marcowith, A., Hennebelle, P., & Ferrière, K. 2016, A&A, 590, A8
Padovani, M., Marcowith, A., Sánchez-Monge, Á., Meng, F., & Schilke, P. 2019, A&A, 630, A72
Padovani, M., Ivlev, A. V., Galli, D., et al. 2020, Space Sci. Rev., 216, 29
Padovani, M., Bialy, S., Galli, D., et al. 2022, A&A, 658, A189
Padovani, M., Galli, D., Scarlett, L. H., et al. 2024, A&A, 682, A131
Pattle, K., Ward-Thompson, D., Berry, D., et al. 2017, ApJ, 846, 122
Pazukhin, A. G., Zinchenko, I. I., Trofimova, E. A., Henkel, C., & Semenov, D. A. 2023, MNRAS, 526, 3673
Peterson, D. E., & Megeath, S. T. 2008, in Handbook of Star Forming Regions, Volume I, 4, ed. B. Reipurth, 590
Redaelli, E., Bovino, S., Giannetti, A., et al. 2021a, A&A, 650, A202
Redaelli, E., Sipilä, O., Padovani, M., et al. 2021b, A&A, 656, A109
Redaelli, E., Bovino, S., Sanhueza, P., et al. 2022, ApJ, 936, 169
Redaelli, E., Bovino, S., Lupi, A., et al. 2024, A&A, 685, A67
Rieke, G. H., & Lebofsky, M. J. 1985, ApJ, 288, 618
Rivilla, V. M., Martín-Pintado, J., Sanz-Forcada, J., Jiménez-Serra, I., & Rodríguez-Franco, A. 2013, MNRAS, 434, 2313
Sabatini, G., Giannetti, A., Bovino, S., et al. 2019, MNRAS, 490, 4489
Sabatini, G., Bovino, S., Giannetti, A., et al. 2020, A&A, 644, A34
Sabatini, G., Bovino, S., Sanhueza, P., et al. 2022, ApJ, 936, 80
Sabatini, G., Bovino, S., & Redaelli, E. 2023, ApJ, 947, L18
Salas, P., Rugel, M. R., Emig, K. L., et al. 2021, A&A, 653, A102
Sanhueza, P., Jackson, J. M., Foster, J. B., et al. 2012, ApJ, 756, 60
Sipilä, O., Caselli, P., & Harju, J. 2015, A&A, 578, A55
Socci, A., Hacar, A., & Bonanomi, F., et al. 2024, A&A, submitted
Spitzer, Lyman, J., & Tomasko, M. G. 1968, ApJ, 152, 971
Stone, E. C., Cummings, A. C., Heikkila, B. C., & Lal, N. 2019, Nat. Astron., 3, 1013
Tafalla, M., Myers, P. C., Caselli, P., Walmsley, C. M., & Comito, C. 2002, ApJ, 569, 815
Tafalla, M., Usero, A., & Hacar, A. 2021, A&A, 646, A97
Tafalla, M., Usero, A., & Hacar, A. 2023, A&A, 679, A112
Tanabe, Y., Nakamura, F., Tsukagoshi, T., et al. 2019, PASJ, 71, S8
Tobin, J. J., Bergin, E. A., Hartmann, L., et al. 2013, ApJ, 765, 18
van der Tak, F. F. S., & van Dishoeck, E. F. 2000, A&A, 358, L79
van der Tak, F. F. S., Black, J. H., Schöier, F. L., Jansen, D. J., & van Dishoeck, E. F. 2007, A&A, 468, 627
Vasyunina, T., Vasyunin, A. I., Herbst, E., & Linz, H. 2012, ApJ, 751, 105
Wakelam, V., Herbst, E., Loison, J. C., et al. 2012, ApJS, 199, 21
Walmsley, C. M., Flower, D. R., & Pineau des Forêts, G. 2004, A&A, 418, 1035
Watson, W. D. 1974, ApJ, 188, 35
Wenger, M., Ochsenbein, F., Egret, D., et al. 2000, A&AS, 143, 9
Wilson, T. L., & Rood, R. 1994, ARA&A, 32, 191
Zielinski, N., & Wolf, S. 2022, A&A, 659, A22

Appendix A: Additional maps

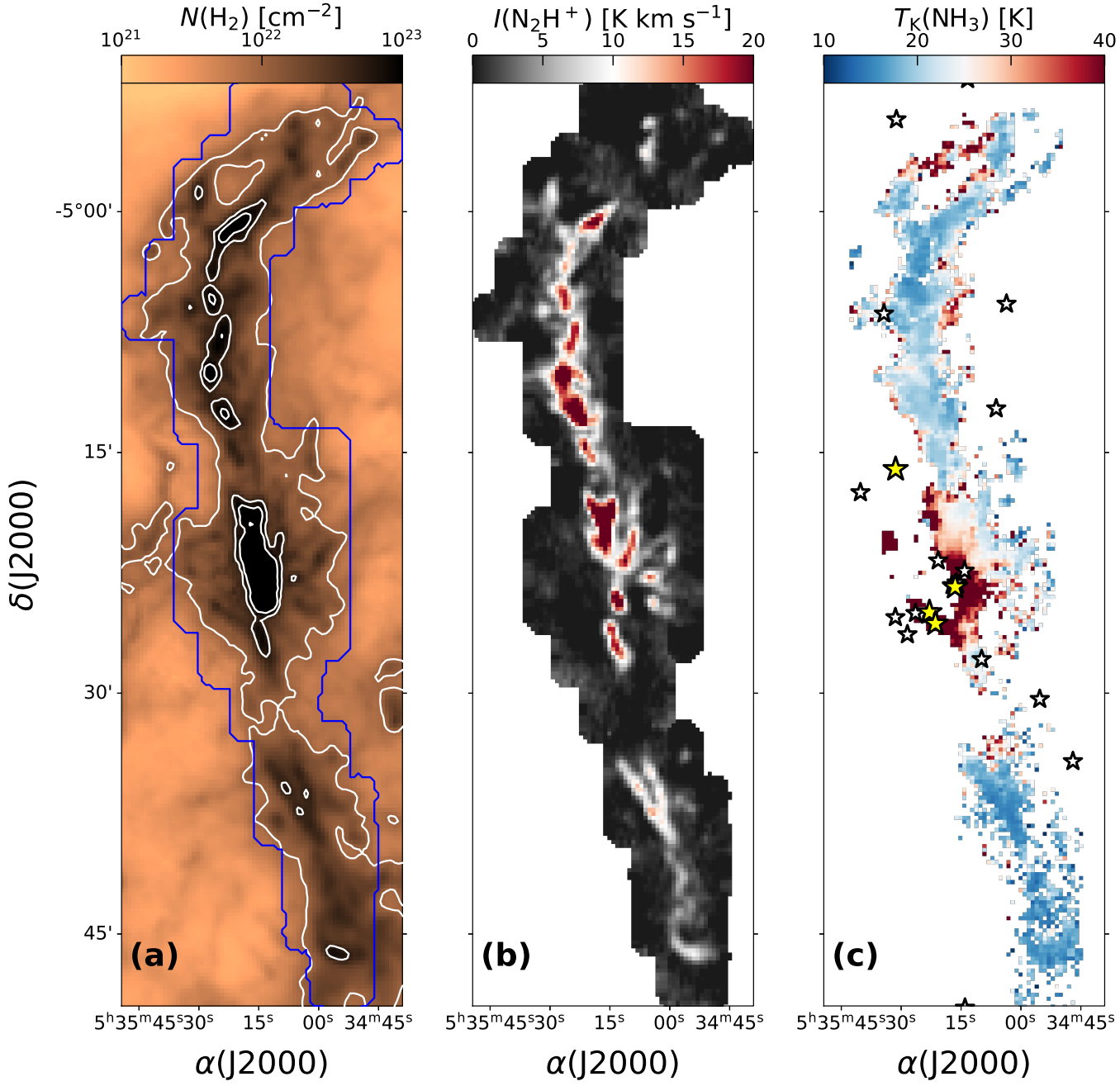

Fig. A.1. ISF as seen in different types of emission. **Panel (a)**: Column density map of H_2 ($N(H_2)$) obtained from dust opacity *Herschel+Planck* observations at 850 μm (Lombardi et al. 2014). The white contours correspond to $[10^{22}, 5 \times 10^{22}, 10^{23}]$ cm^{-2}, and the blue contour represents the footprint of our IRAM-30m observations. **Panel (b)**: N_2H^+ (1–0) integrated-intensity map of observed with IRAM-30m at a resolution of 30″ (see Hacar et al. 2017, for additional information). **Panel (c)**: Kinetic temperature of the gas (T_K) obtained from observations of the two inversion transitions NH_3 (1,1) and NH_3 (2,2) at 32″ with the GBT (Friesen et al. 2017). The white and yellow stars represent the B- and O-type stars in the region, respectively, as in Fig. 1, panel (b).

Figure A.1 shows the OMC-1/-2/-3/-4 regions as seen through the total column density of H_2 (panel a; Lombardi et al. 2014) through the N_2H^+ (1–0) integrated emission (panel b; Hacar et al. 2017) and through the kinetic temperature (panel c; Friesen et al. 2017). The latter was directly delivered by the authors alongside with the corresponding error[4], while the other two were computed as follows:

– $N(H_2)$. We first determined the visual extinction in the K band (A_K) from the dust opacity at 850 μm (τ_{850}),

$$A_K = \gamma \times \tau_{850} + \delta, \tag{A.1}$$

where $\gamma = 2460$ mag and $\delta = 0.012$ mag for Orion A[5]. Then

[4] https://greenbankobservatory.org/science/gbt-surveys/gas-survey-2/

[5] The linear correlation between the two parameters holds for most of Orion A, except for the region close to the Trapezium stars. Since we excluded OMC-1 from the analysis, we can safely apply Eq. (A.1) for our study (see Lombardi et al. 2014, for a full discussion).

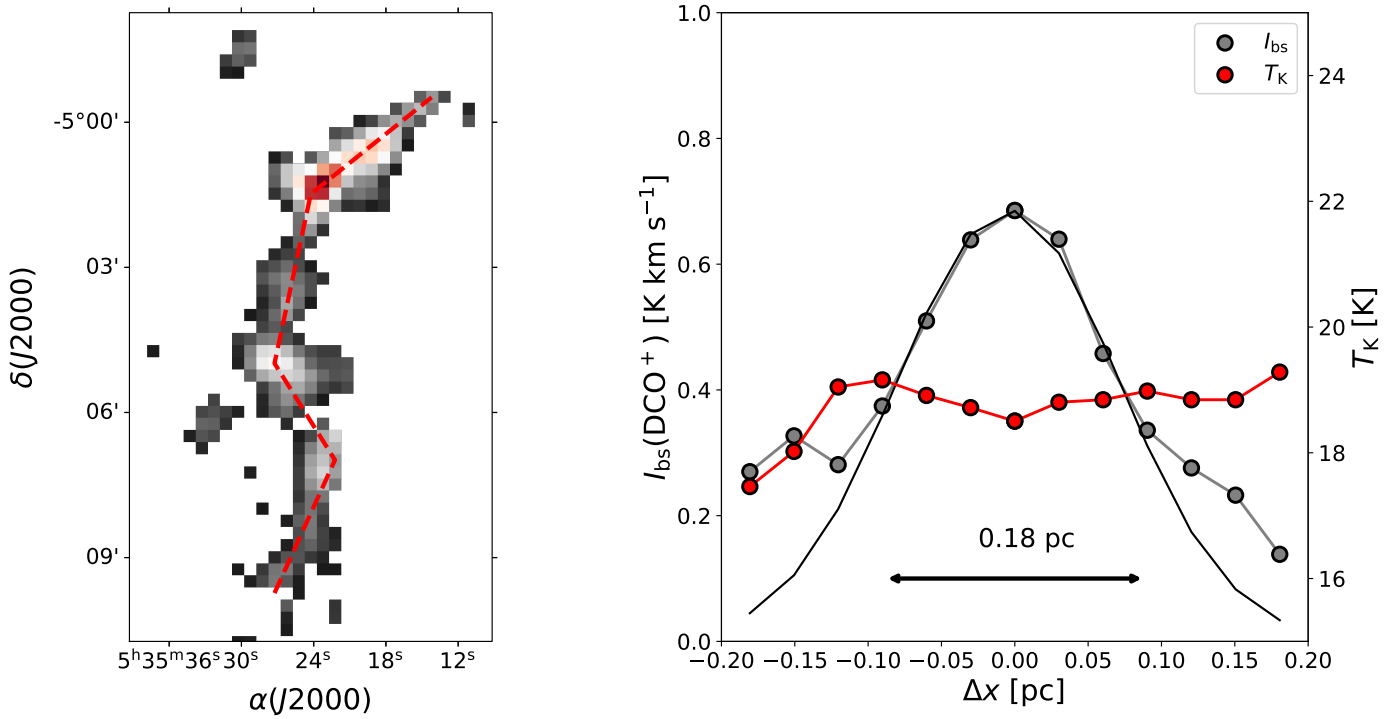

Fig. A.2. Radial profile sampling of the DCO^+ integrated intensity in OMC-2 and OMC-3. **Left panel**: Integrated-intensity map of DCO^+ (3–2) (see also Fig. 1), masked based on the criteria discussed in Sects. 3.2,4.1. The dashed red line represents the axis used for the radial sampling. **Right panel**: Average intensity (I_{bs}) and temperature (T_K) radial profiles computed across the red line in the left panel. The Gaussian best fit to the profile is also displayed (solid black line), along with the derived FWHM (solid arrow).

we converted the extinction in the K band into visual extinction (A_V) using $A_K/A_V = 0.112$ (Rieke & Lebofsky 1985). Finally, we obtained $N(H_2)$ using the conversion (Bohlin et al. 1978)

$$N(H_2) = 0.94 \times 10^{21} \times A_V \text{ cm}^{-2}. \quad (A.2)$$

The corresponding error on the column density of H_2 per pixel was computed following the same procedure and using the error on τ_{850}.

– $I(N_2H^+)$. The intensity map of N_2H^+ (1–0) was obtained by integrating all the hyperfine components of the line (e.g. Caselli et al. 1995) in the velocity range $\Delta V_{lsr} = [-5, 20]$ km s^{-1}.

Figure A.2 shows the radial sampling results onto the DCO^+ (3–2) integrated-intensity map to determine the path length l (see Sect. 5). To perform the radial profile fitting, we employed the following approach: We first masked the integrated-intensity map using the same criteria as applied in Sects. 3.2,4.1. We then subtracted a baseline of $3 \times \sigma(DCO^+)$ from the profile (obtaining I_{bs}). Third, we drew the axis manually onto the map following the emission peaks. Fourth, we sampled all four segments with perpendicular cuts spaced by θ_{beam}, and we sampled the map along each cut every pixel (i.e. every $\theta_{beam}/2$). We finally averaged the four profiles and fit the resulting radial profile with a Gaussian function. The average profile width is FWHM = 0.18 ± 0.15 pc.

Appendix B: Scaling relation of the deuteration fraction

Figure B.1 shows the correlation between R_D and T_K in our study and in comparison with previous estimates. To reduce the scatter of our fields, we sampled the median value, with corresponding IQR, of both R_D and T_K in bins of one Kelvin within 14–25 K (red circles and error bars, respectively). Then, we fitted these 11 median values with a power-law dependence of the form $R_D = R_D^0 \times (T_K/10\,\text{K})^a$, where 10 K was chosen as arbitrary normalisation temperature. The best fit to this dependence reads

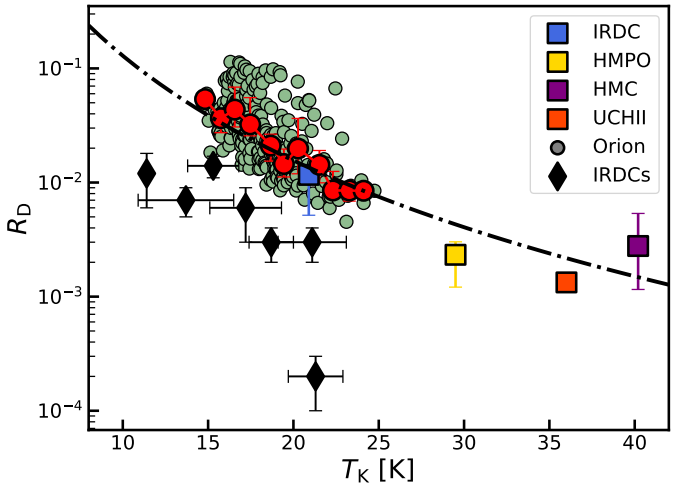

Fig. B.1. Estimates of $R_D = N(DCO^+)/N(HCO^+)$ and T_K across different studies: estimates in Orion, both single fields and median per bin (green and red circles, respectively; this study), in IRDCs (black diamonds; Miettinen et al. 2011), in high-mass star-forming regions (colour-coded squares; Gerner et al. 2014, 2015, see text for discussion on T_K). The black line represents the best fit to the median values of our estimates in Orion and it is exemplified by Eq. B.1.

as follows (black line):

$$R_{\rm D} = 0.24 \times \left(\frac{T_{\rm K}}{10\ {\rm K}}\right)^{-3.8}, \tag{B.1}$$

suggesting variations of two orders of magnitude already within ∼10–40 K, which is the temperature range seen across the ISF (see Fig. A.1, panel c).

To further asses the reliability of this scaling relation, we directly compared the scaling relation determined with deuteration fractions from previous studies. To perform an homogeneous comparison, we selected deuteration fractions determined as $N(\rm DCO^+)/N(\rm HCO^+)$ and with an independent measurement of $T_{\rm K}$. Thus, the first comparison is against the estimates of $R_{\rm D}$ and $T_{\rm K}$ in massive clumps embedded within IRDCs (black diamonds in Fig. B.1; Miettinen et al. 2011, Tables 5-9). The deuteration fractions in these clumps shows a similar scaling with the temperature as our estimates in Orion, up to ∼22 K. While the scaling is similar, the absolute values are lower by a factor of ∼5 on average, which suggests an enhancement of $\rm HCO^+$ deuteration in our fields. Given the similar resolution in the observations (∼20″ − 30″), column density (∼10^{22} − 10^{23} cm^{-2}) and volume density (∼$0.3 - 2 \times 10^5$ cm^{-3}) in the two studies, these higher deuteration fractions might be connected to overall warmer temperatures in our fields, and maybe to unresolved depletion and density gradients within the massive clumps (Miettinen et al. 2011).

We also explored whether the variation in deuteration fraction is connected to the star-formation regime of the region. Thus, the second comparison was made with the estimates of $R_{\rm D}$ and $T_{\rm K}$ in high-mass regions in different evolutionary stages (i.e. High-Mass Protostellar Objects (HMPO), Cores (HMC) and Ultra-Compact HII regions (UCHII), colour-coded squares in Fig. B.1; Gerner et al. 2015). We gathered the column densities of $\rm DCO^+$ and $\rm HCO^+$ from CDS[6], computed the median and IQR per evolutionary stage, and associated their average kinetic temperature determined from the chemical models of Gerner et al. (2014)[7]. Despite their different evolutionary stages, the high-mass regions all agree very well with the scaling relation determined in Eq. B.1. The prime factor driving the decrease in $R_{\rm D}(\rm HCO^+)$ in molecular clouds therefore appears to be $T_{\rm K}$, while other factors, such as the star-formation history of the regions, affect its variation only marginally.

[6] https://cdsarc.cds.unistra.fr/viz-bin/cat/J/A+A/579/A80

[7] Gerner et al. (2015) also provided updated kinetic temperatures for a chemical network including deuterated species. However, their models did not significantly improve the results of Gerner et al. (2014) and still did not converge for some of the molecular species in the chemical network. Thus, we opted for the $T_{\rm K}$ from Gerner et al. (2014) given the more general set of reactions considered.